Chemistry
A European
Journal

Chemistry Europe
European Chemical Societies Publishing

Accepted Article

Title: Rapid Aqueous Synthesis of Large-size and Edge/Defect-rich Porous Pd and Pd-alloyed Nanomesh for Electrocatalytic Ethanol Oxidation

Authors: Yuxiang Teng, Ke Guo, Dongping Fan, Hongyou Guo, Min Han, Dongdong Xu, and Jianchun Bao

To be cited as: *Chem. Eur. J.* 10.1002/chem.202101144

Link to VoR: https://doi.org/10.1002/chem.202101144

WILEY-VCH

10.1002/chem.202101144

WILEY-VCH

FULL PAPER

Rapid Aqueous Synthesis of Large-size and Edge/Defect-rich Porous Pd and Pd-alloyed Nanomesh for Electrocatalytic Ethanol Oxidation

Yuxiang Teng, Ke Guo, Dongping Fan, Hongyou Guo, Min Han, Dongdong Xu,* Jianchun Bao

Y. Teng, K. Guo, D. Fan, H. Guo, Prof. M. Han, Prof. D. Xu, Prof. J. Bao
Jiangsu Key Laboratory of New Power Batteries, Jiangsu Collaborative Innovation Center of Biomedical Functional Materials, School of Chemistry and Materials Science, Nanjing Normal University, Nanjing, Jiangsu 210023, China.
E-mail: ddxu@njnu.edu.cn (D. Xu)
Supporting information including the synthesis, electrocatalytic tests and characterization details of Pd and Pd-based nanomesh, and supporting electron microscopy images and electrocatalytic performance for this article is given via a link at the end of the document.

Abstract: In this work, we utilized a facile aqueous synthesis strategy (finished in 5 min at room temperature) to produce large-size Pd, PdCu, and PdPtCu nanomesh without additional organic ligands or solvent and the volume restriction of reaction solution. The obtained metallic nanomesh possess graphene-like morphology and a large size of dozens of microns. Abundant edges (coordinatively unsaturated sites, steps, and corners), defects (twins), and mesopores exhibited in the metallic ultrathin structures. The formation mechanism for porous Pd nanomesh disclosed that they undergo the oriented attachment growth along <111> direction. Owing to the structural and compositional advantages, PdCu porous nanomesh with certain elemental ratio (e.g., $Pd_{87}Cu_{13}$) presented enhanced electrocatalytic performance (larger mass activity, better CO tolerance and stability) toward ethanol oxidation.

Introduction

Fuel cells have been anticipated as sustainable energy source to afford reliable power in many fields (e.g., portable devices and electric vehicles).[1] As the primary unit in fuel cells, the electrocatalysts usually determine the electrochemical performance of practical devices. Designing and synthesizing high-efficiency electrocatalysts with enhanced intrinsic activity and/or abundant active sites become the key issue in the field of energy chemistry.[2] Platinum group elements have proved to be the best choice in both anode and cathode catalytic reactions owning to their superior electrochemical performance.[3] A desired electrocatalyst may combine multiple advantages, including abundant active sites (or high atomic efficiency), optimized electronic structure, and desired geometric architecture. For example, by means of tuning the crystalline structure, morphology, and composition, Pd and Pd-based alloys in the shape of nanoparticles, nanowires, nanosheets, porous nanospheres, nanoframes, and single-atom have been widely synthesized and exhibited superior electrocatalytic performance toward small molecules (hydrogen, ethanol, methanol, and formic acid) oxidation, hydrogen evolution, oxygen reduction, etc.[4] Furthermore, other efficient factors (e.g., supports, defects/strain, heterojunction) should be carefully considered for the improvement of electrocatalytic activity and stability.[5] For instance, the intrinsic surface strain in Pd nanosheets with five monolayers can be finely tuned and resulted in enhanced reactivity in ORR and HER.[6]

Numerous studies focus on the construction of ultrathin two-dimensional Pd and Pd-based nanosheets with special crystalline structures/morphologies to boost their electrocatalytic performance. Most of the synthesis resort to the presentation of carbon monoxide to restrict the crystalline growth of face-centered cubic Pd along <111> orientation.[7] Via the precise control of synthesis parameter, the thickness, size, porosity, edge sites, crystallinity, and defects of Pd nanosheets could be tailored to enhance their intrinsic electrocatalytic activity.[8] Rich edges in Pd nanosheets can create abundant low-coordinated atoms, corners, and steps, stacking faults, and grain boundaries, which greatly contributed to obtain a high CO faradaic efficiency in CO_2 electroreduction.[8d, 8e] The introduction of mesopores into Pd nanosheets (e.g., Pd nanomesh) is an effective means to expose more active sites and boost the electrocatalytic activity toward ethanol oxidation reaction (EOR).[8b] When combining the advantages of defects-rich, porous, and sub-nanometer features, Wang and co-works presented that Pd metallene exhibited superior ORR mass/specific activity and stability.[8c] From above cases, we can conclude that more structural and compositional advantages should be designed into one electrocatalysts in order to boost the corresponding electrocatalytic performance. Furthermore, simplifying the synthesis pathway and reducing the cost represents another research interest.

Herein, we reported a facile rapid aqueous synthesis of lager-size, edge/defect-rich porous Pd and Pd-alloyed nanomesh (e.g., PdCu and PdPtCu). The synthesis was realized under the presence of H_2PdCl_4, CO, H_2O, and KOH at room temperature. There were no additional ligands and the limitation of reaction solution volume. The obtained porous Pd nanomesh (denoted as Pd PNM) possess abundant mesopores and defects with a size of dozens of microns along the plane direction. The oriented attachment growth along <111> orientation was proposed for the formation mechanism of Pd PNM. Owning to the multiply advantages (large-size, ultrathin, edge/defect-rich, and porous) in PdCu PNM, $Pd_{87}Cu_{13}$ PNM exhibited enhanced electrocatalytic mass activity, anti-poisoning ability, and stability toward EOR. The corresponding enhanced mechanism based on structural and compositional advantages was carefully discussed. This synthesis strategy may be extended to prepare other Pd-based alloys and the obtained materials utilized in other kinds of electrocatalytic reactions.

10.1002/chem.202101144

Results and Discussion

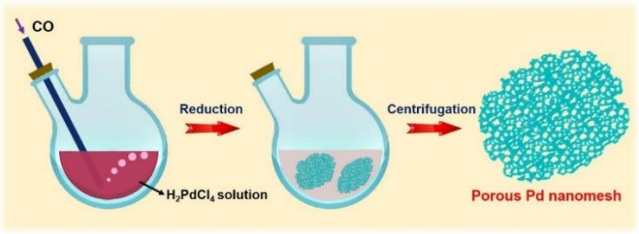

Figure 1 Schematic illustration for the synthesis of large-size porous Pd nanomesh in the aqueous solution via the reduction of CO gas.

The porous Pd nanomesh were successfully prepared under a very facile synthesis condition as described in Experimental section and schemed in Figure 1. Carbon monoxide (CO) gas with an optimized flow rate was bubbled into the H_2PdCl_4 solution where KOH was utilized to control the pH value of reaction system. In the synthesis, CO acted as the reduction agent and the overall reaction process could be finished in 5 min under room temperature. No additional ligands were employed and the volume of reaction solution could be easily extended to several liter. There is also no limitation of the kinds of reaction vessels. Therefore, we realized the facile, rapid, low-cost, and large-scale synthesis of porous Pd nanomesh in this work. Via the addition of other metallic precursors (e.g., $CuCl_2$ and H_2PtCl_6), this synthesis strategy also succeeded in the production of Pd-based alloys (for example, PdCu, PdPt, and PdPtCu nanomesh) with tailored compositional ratio.

The morphology and crystallographic structure of obtained porous Pd nanomesh were carefully characterized by transmission electron microscopy (TEM). As shown in Figure 2a-b and S1, Pd nanomesh possess graphene-like two-dimensional morphology with lots of wrinkles and a large size of dozens of microns along the plane orientation. High-magnification observation displayed that Pd PNM consist of thin network Pd crystals with the diameter around 2-6 nm (Figure 2c). Numerous mesopores formed among the frameworks. The thickness of Pd PNM was measured to be ~3.5 nm taken from the standing fringe (Figure 2d), confirming its ultrathin feature. Compared to solid nanosheets, our Pd PNM could produce rich edges owning to the thin diameter/thickness and abundant mesopores. Selected area electron diffraction (SAED) captured on free-standing Pd PNM presented a set of diffraction patterns (the insert in Figure 2c), indexed to the (111), (200), (220), and (311) planes of fcc Pd crystallographic structure, indicating the polycrystalline nanostructures. The detailed crystallographic structures were carefully checked by high-resolution TEM observations (Figure 2e). Some facets with the *d*-spacing value of 0.197 and 0.229 nm which could be ascribed to (200) and (111) of Pd crystals were observed. The corresponding fast Fourier transformation (FFT) pattern exhibited the crystallographic [110] observation direction (the insert in Figure 2e). As reported before, common Pd nanosheets prepared by CO usually exposed (111) planes because CO molecules can strongly adsorb on (111) planes of Pd crystals.[2b, 7a] Therefore, the formation of Pd PNM in this work may possess another different formation mechanism (discussed later). Interestingly, along with the rich edges inside Pd PNM, abundant coordinatively unsaturated sites, steps, corners, and twins could be obviously noticed (Figure 2e, S2-3). These structural features would greatly enhance the intrinsic electrocatalytic activity of general nanoelectrocatalysts. The wide-angle X-ray diffraction (XRD) pattern also verified the *fcc* Pd PNM nanostructures with a set of diffraction peaks corresponded to (111), (200), (220), (311), and (222) facets (Figure 2f). All above characterizations demonstrated that obtained Pd PNM hold many advanced structural features like ultrathin (both in diameter and thickness), large-size, porous, edge/defect-rich, ligand-free, and so on.

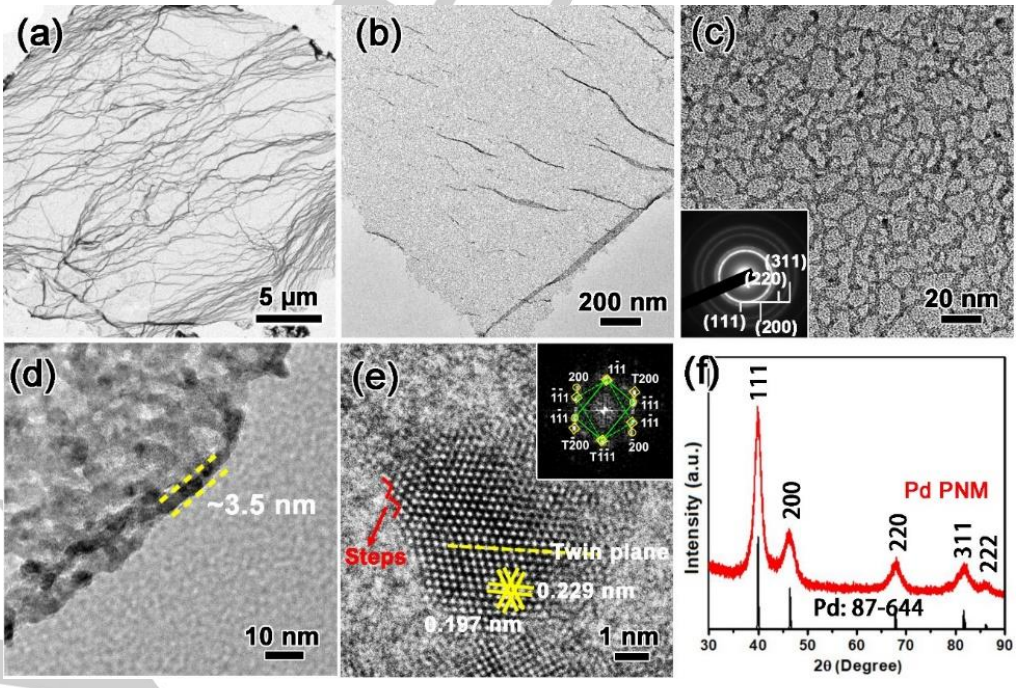

Figure 2. (a-c) TEM images with different magnification, (d) TEM image from the cross section, (e) HRTEM image, and (f) XRD pattern of porous Pd nanomesh. The inserts in (c) and (e) are the corresponding SAED and FFT patterns, respectively.

10.1002/chem.202101144

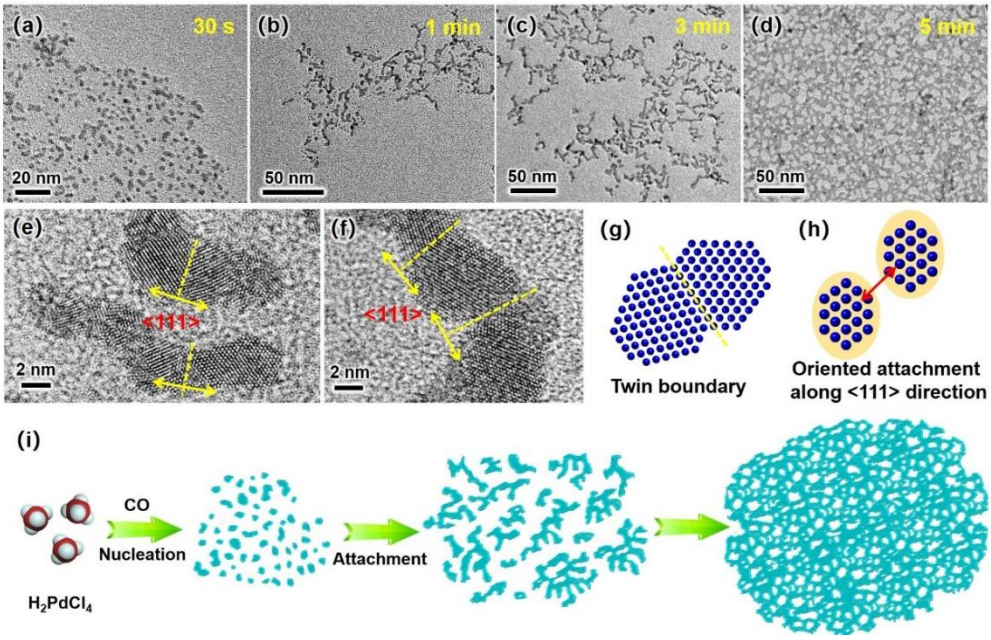

Figure 3. (a-d) TEM images of Pd crystals obtained at different growth period. (e-f) Typical HRTEM images of Pd products in (b). (g) Schematic illustration for Pd twin boundary and (h) oriented attachment growth along <111> direction. (i) Proposed formation mechanism of Pd PNM via the oriented attachment growth along the plane orientation.

Although the overall preparation process for Pd PNM was very rapid, we managed to capture the metallic intermediates and carefully characterized their nanostructures. From TEM observation, we can find that abundant small nanocrystals formed during the initial reduction stage (less than 30 s, Figure 3a). Then, these nanocrystals attached to each other to produce network morphology only along the plane orientation (Figure 3b-c). After repeating the attachment process, large-size 2D nanomesh were emerged only in 5 min (Figure 3d). Plentiful mesopores were well created inside the network Pd framework. We also checked the crystallographic structure of these intermediates (e.g., in 1 min) via TEM observation. As shown in Figure 3e and f, these initial small crystals generally attached to each other along the <111> direction, resulting in abundant (111) twin planes as also presented in Figure 2e and S3. The oriented attachment growth process was a common phenomenon in the production of many metallic nanostructures.[9] Especially in the *fcc* nanocrystals (e.g., Pd and Au),[10] twin boundary along the (111) planes was often seen after the oriented growth (Figure 3g and h). The crystallographic growth along <111> direction may reduce the surface energy and produce the thermodynamically stable morphology and nanostructures. Based on the TEM observation, a mechanism for the formation of Pd PNM via the oriented attachment growth along the plane orientation were proposed (Figure 3i). Lots of small Pd crystals generated in the initial reduction period and attached to each other along the specific facets to produce large network Pd nanomesh. No additional ligands were utilized to direct the formation of two-dimensional Pd nanostructures.

As we all know, the exposed (111) facets and more thin thickness (less than 2 nm) were usually found in the common Pd nanosheets synthesized under CO condition as reported everywhere.[2b, 7a] In order to further verify the formation mechanism of Pd PNM deeply, a serial of control experiments was performed. First, the concentration of precursor H_2PdCl_4 was changed from 0.6 to 1.4 mL. Large-size Pd nanomesh similar with the ones in Figure 1 were obtained (Figure S4), indicating the concentration of H_2PdCl_4 was not the key factor in this synthesis. The synthesis under different CO flow rate (the amount of reduction agent) also produce well Pd PNM where no obvious distinction in morphology was observed (Figure S5). A low CO flow rate of 0.05 L/min was proved to be enough for the reduction and subsequent crystalline growth of Pd PNM. Second, we found that reaction temperature could greatly tailor the morphology of Pd products. Under the low temperature (0 °C), only poor large-size Pd nanosheets assembled from small nanosheets were obtained (Figure S6a and b). Higher temperature (e.g., 50 and 70 °C) could result in irregular aggregates of large Pd nanoparticles (Figure S6c-f). Lower reaction temperature may generate a small number of crystal nuclei in the initial stage and these nuclei slowly grew into bigger solid nanosheets via the diffusion-limited aggregation and further large-size porous nanomesh based on the oriented attachment process. Correspondingly, higher reaction temperature would produce lots of crystal nuclei and easily result in thermodynamically stable irregular aggregates in a short reaction time. Third, we found that pH value of the reaction solution was the important factor for the construction of Pd PNM. Well-defined Pd PNM could be obtained only with the pH value around 11 (Figure S7). Higher pH gave agglomerated nanosheets (Figure S7f). Lower pH media could direct the formation of ultrathin Pd nanosheets with exposed (111) planes but fail to build large-size PNM as reported before.[7a] In acidic condition, the precursor H_2PdCl_4 can be reduced rapidly by CO. CO molecules strongly adsorbed on the Pd (111) planes and produced hexagonal Pd nanosheets. The relatively slow reduction rate in alkaline condition facilitated the Pd nuclei to connect to each other along specific crystalline orientation, for example, <111> direction in Pd PNM. In this condition, CO

10.1002/chem.202101144

molecules only played the role of reduction agent. Based on above control experiments, we proposed the oriented attachment growth along <111> direction for the formation mechanism of Pd PNM only under proper synthesis parameter, especially the reaction temperature and pH value.

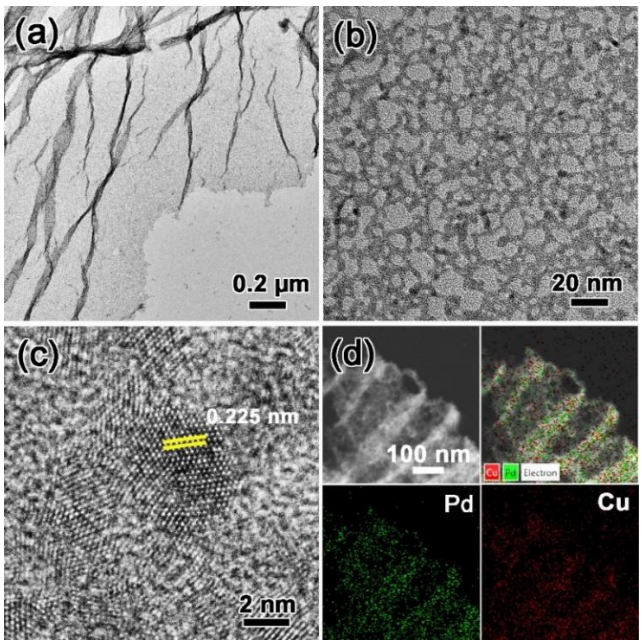

Figure 4. (a) Low- and (b) high-magnification TEM images, (c) high-resolution TEM image, and (d) HAADF-STEM and elemental mapping of $Pd_{87}Cu_{13}$ PNM.

The rapid and facile synthesis for Pd PNM could be also easily extended to Pd-based alloys. PdCu PNM with different elemental ratio were prepared under the similar synthesis condition with the additional precursor of $CuCl_2$. For example, $Pd_{87}Cu_{13}$ PNM with large-size and edge-rich feature as Pd PNM could be confirmed by TEM observation (Figure 4a and S8). Abundant mesopores were also located inside the network metallic nanostructures (Figure 4b). Similar crystallographic structure, including *fcc* crystalline facets, rich edges, abundant steps, and twins, could be easily found (Figure 4c), no obvious distinction with Pd PNM except for the smaller interlattice of (111) facet (0.225 nm). High-angle annular dark-field scanning TEM (HAADF-STEM) and mapping images displayed the homogeneous distribution of Pd and Cu elements in PdCu PNM (Figure 4d). The compositional ratio was calculated to be 87: 13 based on energy disperse spectroscopy (EDS), similar with the data from inductively coupled plasma atomic emission. The above characterization confirmed the successful formation of $Pd_{87}Cu_{13}$ PNM. Additionally, PdCu PNM with different ratio (e.g., $Pd_{81}Cu_{19}$ and $Pd_{96}Cu_4$) were also prepared as showed in Figure S9 and 10. However, when the content of Cu precursors was further increased, poor nanomesh could be only obtained (Figure S11). More Cu in the synthesis shall decrease the reduction kinetics, resulting in irregular crystalline growth and finally poor morphology. Besides, we also succeeded in the preparation of ternary metallic alloy (e.g., $Pd_{78}Pt_7Cu_{15}$ PNM, Figure S12), further confirming the universality of this synthesis strategy for the construction of large-size porous metallic nanomesh.

The crystallographic structures and electron state of $Pd_{87}Cu_{13}$ PNM were further checked by wide-angle X-ray diffraction (XRD) and X-ray photoelectron spectroscopy (XPS). Only a set of diffraction peaks from XRD patterns could be found in three PdCu PNM (Figure 5a). The peaks were well indexed to (111), (200), (220), (311), and (222) facets of *fcc* PdCu PNM. Along with the increase of Cu content, an obvious shift to higher angles were observed from standard Pd (JCPDS 87-644) to Cu (JCPDS 70-3038) side (Figure S13). The shift in diffraction peak disclosed the successful alloying of elemental Cu into Pd framework. Due the smaller atomic radius of Cu, PdCu PNM exhibited shrunken interlattices compared to pure Pd PNM as presented in Figure 2f. High-resolution XPS spectra of Pd 3d and Cu 2p were tested to check the elemental states of PdCu PNM. Major Pd^0 and minor Pd^{2+} species were found in Pd 3d spectra (Figure 5b). The binding energies of Pd^0 3d3/2 and 3d5/2 were measured to be 341.0 and 335.7 eV, respectively, positively shifted (~0.6 eV) compared to pure Pd PNM (340.4 and 335.1 eV). In the Cu 2p spectra, major metallic state Cu^0 species were also found with the value of 951.8 and 932.1 eV for Cu 2p1/2 and 2p3/2, respectively, negatively shifted to pristine Cu (952.2 and 932.6 eV). The shifts in both Pd and Cu verified the strong interaction between Pd and Cu, resulting the uneven distribution of electrons owing to the electron transfer from Pd to Cu.[11] The downshift of d-band center in Pd could promote desorption of poisoning intermediates on the surface of Pd, which was beneficial for the electrocatalytic EOR process (discuss later).

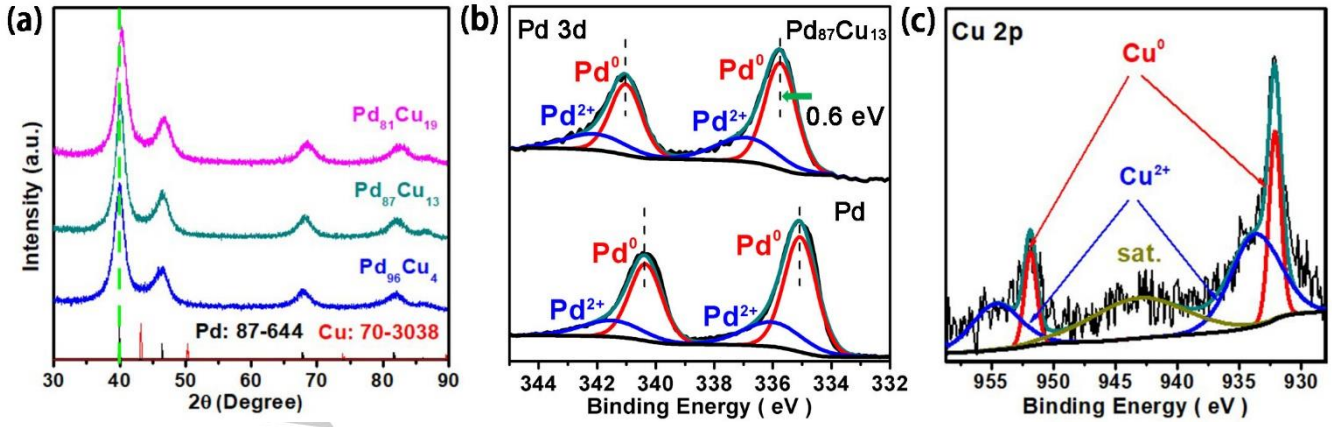

Figure 5. (a) Wide-angle XRD patterns of $Pd_{87}Cu_{13}$ PNM with distinct elemental ratio. (b) High-resolution XPS spectras of Pd 3d of $Pd_{87}Cu_{13}$ and Pd PNM. (c) XPS spectra of Cu 2p of $Pd_{87}Cu_{13}$.

10.1002/chem.202101144

Above obtained Pd and PdCu PNM exhibited multiple structural and compositional features, such as ultrathin, large-size, porous, edge/defect-rich, ligand-free, alloyed and so on. EOR was employed to evaluate these advantages in electrocatalytic process. The cyclic voltammograms (CV) of five nanocatalysts, including Pd, $Pd_{81}Cu_{19}$, $Pd_{87}Cu_{13}$, $Pd_{96}Cu_4$ PNM, and commercial Pd nanoparticles (NPs), were first collected in N_2-saturated 1.0 M KOH (Figure 6a). The reduction peaks (negative scans) in the region of -0.5 V and -0.1 V (vs. SCE) were seen due to the reduction of PdO to Pd. Larger peak area and lower potential were found in $Pd_{87}Cu_{13}$ PNM, indicating the presence of more electrocatalytic active sites and easier reduction of PdO to Pd. The electrochemical active surface areas (ECSAs) were calculated based on the coulombic charges for PdO reduction with the values of 20.4, 27.8, 28.0, 23.0, and 19.3 $m^2\ g_{Pd}^{-1}$ for Pd, $Pd_{81}Cu_{19}$, $Pd_{87}Cu_{13}$, $Pd_{96}Cu_4$ PNM, and commercial Pd NPs, respectively (Figure 6b). The enlarged ECSA in $Pd_{87}Cu_{13}$ could be attributed to the higher utilization efficiency of Pd atoms.

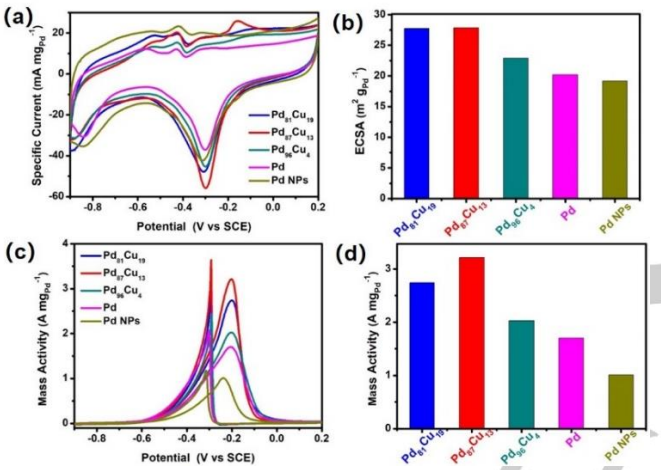

Figure 6. (a) CV curves and (b) the corresponding ECSAs of $Pd_{81}Cu_{19}$, $Pd_{87}Cu_{13}$, $Pd_{96}Cu_4$, Pd PNM, and commercial Pd NPs collected in 1.0 M KOH. (c) CV curves and (d) summarized mass activities of curves of $Pd_{81}Cu_{19}$, $Pd_{87}Cu_{13}$, $Pd_{96}Cu_4$, Pd PNM, and commercial Pd NPs collected in 1.0 M KOH and 1.0 M ethanol.

The enhanced electrocatalytic activity of Pd and PdCu PNM were verified in the ethanol oxidation reaction. As shown in Figure 6c, the CVs of all the nanocatalysts in 1.0 M KOH and 1.0 M ethanol displayed distinct peaks compared to the ones collected in 1.0 M KOH. The peaks in the forward scan were ascribed to the electrochemical oxidation of ethanol and the backward scan to further oxidation/removal of the reaction intermediates. It was found that $Pd_{87}Cu_{13}$ PNM possess lowest onset potential and largest mass activity compared to other nanocatalysts. The mass activity of $Pd_{87}Cu_{13}$ PNM was measured to be 3.22 A mg_{Pd}^{-1} (Figure 6d), 1.2, 1.6, 1.9 and 3.2-fold than $Pd_{81}Cu_{19}$ PNM (2.72 A mg_{Pd}^{-1}), $Pd_{96}Cu_4$ PNM (2.04 A mg_{Pd}^{-1}), Pd PNM (1.70 A mg_{Pd}^{-1}), and commercial Pd NPs (1.01A mg_{Pd}^{-1}), respectively. The enhanced mass activity in $Pd_{81}Cu_{19}$ PNM was mainly attributed to the synergistical effect of structural and compositional advantages.

Electrocatalytic stability/durability was an important concern for the preparation of good electrocatalysts. In the common EOR process, the further oxidation/removal of CO_{ads} or CH_3CO_{ads} intermediates (the rate-determining step) usually regulated the overall electrocatalytic efficiency. CO stripping tests were performed to check the anti-poisoning ability for the desorption of carbonaceous intermediates in these electrocatalysts. The successive CV curves collected in 1.0 M KOH displayed that most of CO molecules had been removed after the second scanning. However, in the first scanning, $Pd_{87}Cu_{13}$ PNM exhibited more negative onset potential and larger active areas compared to other four catalysts (Figure 7a), indicating superior capacity for the removal of CO_{ads} or better CO tolerance. Furthermore, current-time (*i-t*) chronoamperometry measurements were also utilized to evaluate the durability in the long-term electrocatalytic oxidation. Relatively slow current decay in the initiation stage and the largest residual mass activity were found in $Pd_{87}Cu_{13}$ PNM. The *i-t* chronoamperometry curves also showed the durability sequence as $Pd_{87}Cu_{13}$ PNM > $Pd_{81}Cu_{19}$ PNM > $Pd_{96}Cu_4$ PNM > Pd PNM > Pd NPs, confirming the structural and compositional features in $Pd_{87}Cu_{13}$ PNM as an ideal electrocatalyst again. In addition, the cycling stability of $Pd_{87}Cu_{13}$ PNM and Pd NPs was also explored by means of successive CV scans (Figure 7c and S14). After 500 cycles, $Pd_{87}Cu_{13}$ PNM hold the retained mass activity about 1.62 A mg_{Pd}^{-1} (50% of initial value), higher than Pd NPs (0.22 A mg_{Pd}^{-1}, 33%). All above tests confirmed the enhanced stability/durability for $Pd_{87}Cu_{13}$ PNM toward electrocatalytic EOR. The deactivation of $Pd_{87}Cu_{13}$ PNM in the stability test may be mainly caused by morphological stacking and Ostwald ripening growth. As shown in Figure S15, TEM images of $Pd_{87}Cu_{13}$ PNM after above tests presented obvious stacking of ultrathin nanomesh although most porous and defect features retained. Ostwald ripening growth along different crystallographic direction could easily happen due to the stacking, resulting in the loss of some active sites and thus the partial deactivation.

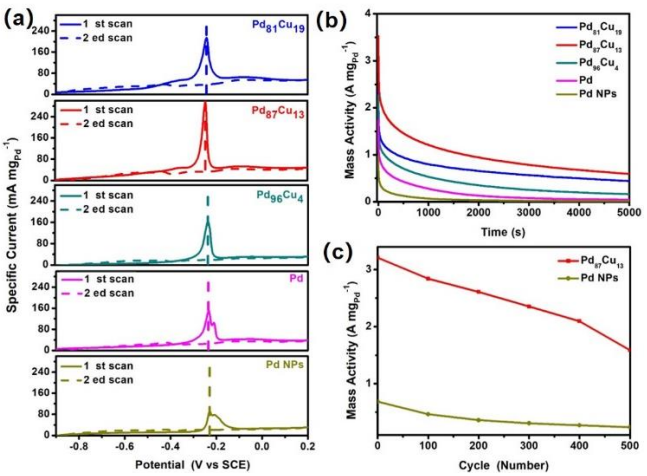

Figure 7. (a) Electrocatalytic CO striping voltammograms collected in 1.0 M KOH at a scan rate of 50 mV s^{-1}. (b) *i-t* chronoamperometry curves collected in 1.0 M KOH and 1.0 M ethanol. (c) The long-term cycling stability curves of $Pd_{87}Cu_{13}$ PNM and commercial Pd NPs.

The abovementioned electrocatalytic tests confirmed the enhanced EOR performance of $Pd_{87}Cu_{13}$ PNM, compared to other catalysts with distinct morphology/structure and composition. It is well known that the EOR on Pd and Pd-based alloys in alkaline media mainly undergoes a dual-pathway mechanism (C1 and C2) where the C2 pathway dominates because the reaction energy barrier is relatively high in the C1 pathway.[12] Especially, as for

PdCu nanocrystals, sufficient in-situ characterizations had confirmed the main reaction mechanism as: [13]

$Pd + CH_3CH_2OH \rightarrow Pd\text{-}(CH_3CH_2OH)_{ads}$

$3OH^- + Pd\text{-}(CH_3CH_2OH)_{ads} \rightarrow Pd\text{-}(CH_3CO)_{ads} + 3H_2O + 3e^-$

$Cu + OH^- \rightarrow Cu\text{-}OH_{ads} + e^-$

$Pd\text{-}(CH_3CO)_{ads} + Cu\text{-}OH_{ads} \rightarrow Pd\text{-}CH_3COOH + Cu$

$Pd\text{-}CH_3COOH + OH^- \rightarrow Pd + CH_3COO^- + H_2O$

Based on above reaction mechanism, we can explain that synergic enhancement effect of structural and compositional advantages in $Pd_{87}Cu_{13}$ PNM resulted in the superior electrocatalytic EOR performance. On the one hand, our synthesis strategy succeeded in the construction of Pd and Pd-alloyed PNM with a great number of structural features, such as ultrathin (both in diameter and thickness), large-size, porous, edge/defect-rich, ligand-free, and so on. These features greatly contributed to the formation of more active sites and the increase of atomic efficiency (Figure 8). Opened 2D framework could facilitate the mass/electron transfer for reactants during the electrocatalysis. The rich coordinatively unsaturated sites along the crystalline edges and defects/twins inside the crystals highly boosted the inherent electrocatalytic activity.[5b, 8b, 8e, 10b] On the other hand, alloying Cu into Pd crystals could further promote the electrocatalytic performance, known as compositional effect. From the above XPS characterization, we realized that the electron transfer in PdCu alloys was beneficial to the desorption of poisoning intermediates (e.g., CH_3CO_{ads}) on the catalytic active Pd sites. Additionally, appropriate Cu content could produce enough $Cu\text{-}OH_{ads}$ which would react/oxidize rapidly with adjacent poisoning intermediates. Therefore, the presence of Cu would greatly accelerate the electrocatalytic kinetics via the optimizing of rate-determining step in EOR. However, the compositional advantage also revealed that appropriate Cu content in PdCu PNM was necessary. Low Cu content may fail to provide enough OH_{ads} and high Cu content relatively reduce the active Pd sites. When the third element (e.g., Pt) was introduced, ternary PdPtCu PNM exhibited higher mass activity compared to binary PdCu PNM and monometallic Pd PNM (Figure S16), further confirming the compositional effect in electrocatalysis.

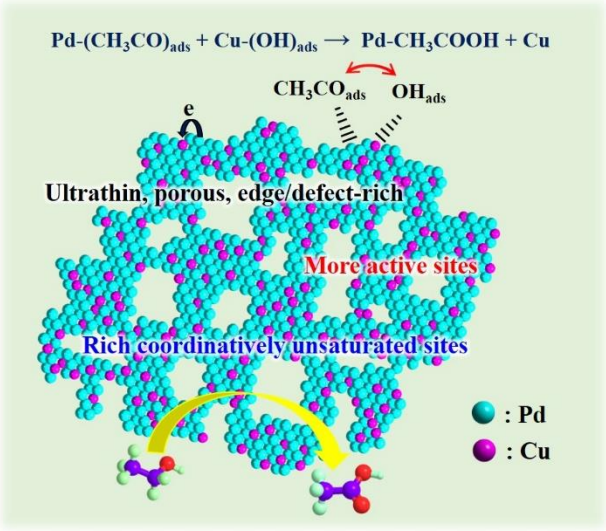

Figure 8. Schematic illustration for enhanced electrocatalytic EOR performance of large-size and edge-rich porous PdCu nanomesh.

Conclusion

In summary, a facile and rapid aqueous synthesis for Pd and Pd-alloyed nanomesh with multiply structural advantages like ultrathin, large-size, porous, edge/defect-rich, ligand-free was realized in this work. No additional ligands was employed and the synthesis could be performed on a large scale. The structural features resulted in more catalytic active sites and high atomic efficiency. Abundant defects (e.g., twins) and coordinatively unsaturated sites could increase the inherent electrocatalytic activity. The engineering of another metal into Pd PNM with controlled ratios further boosted the electrocatalytic performance as compositional effect to tailor the rate-determining step of EOR. Synergic structural and compositional enhancement effects endowed $Pd_{87}Cu_{13}$ PNM with enhanced mass activity, anti-poisoning ability, and stability/durability in electrocatalytic EOR, compared to PdCu PNM with other elemental ratios, Pd PNM, and Pd NPs. The synthesis could be also extended to other composition, for example, ternary PdPtCu PNM, affirming the universality of our synthesis for large-scale and edge-rich metallic nanomesh. The idea to design metallic catalysts with advanced crystalline structures (e.g., defects, porous, and ultrathin) will be helpful for exploring how to boost the intrinsic electrocatalytic activity and further prepare desired and practical electrocatalysts.

Experimental Section

Chemicals. Palladium chloride ($PdCl_2$), cupric chloride ($CuCl_2$), chloroplatinic acid (H_2PtCl_6), potassium hydroxide (KOH), hydrochloric acid (HCl) and ethanol were obtained from Sinopharm Chemical Reagent Co. Ltd. Nafion solution and commercial palladium carbon (Pd/C) were purchased from Alfa Aesar. H_2PdCl_4 solution (10 mM) was prepared by dissolving $PdCl_2$ in HCl solution. All above reagents with analytical reagent grade were used without further purification.

Synthesis of porous Pd and Pd-alloyed nanomesh. In a typical synthesis, 1.0 mL of H_2PdCl_4 solution (10 mM) and 0.5 mL of KOH solution (100 mM) was mixed with 5.0 mL of deionized H_2O in a glass vessel. Then CO gas was bubbled continually into the solution at a rate of 0.40 L/min for 5 min under room temperature (25 °C). The color of solution quickly changed from yellow to black. The final metallic products were collected by centrifugation and washed several times with ethanol/H_2O. As for the synthesis of PdCu and PdPtCu nanomesh, a certain amount of $CuCl_2$ or/and H_2PtCl_6 solution (10 mM) was mixed with H_2PdCl_4 solution and followed by the same process as Pd nanomesh.

Electrochemical ethanol oxidation. The electrocatalytic tests were conducted using a CHI660E electrochemical workstation. All measurements were carried out at room temperature (25 °C). A three-electrodes system (a carbon rod as the counter electrode, a silver/silver chloride electrode as the reference electrode, and a glassy carbon electrode coated with catalysts ink as the working electrode) was utilized for all electrochemical tests. Before the electrocatalytic tests, the work electrode (GCE) was thoroughly cleaned with H_2O/ethanol. To prepare the ink of catalyst, 0.5 mg of catalysts and 2.0 mg of Valcan XC-72 were mixed with 0.4 mL of ethanol and 0.1 mL of H_2O and sonicated for 30 min, then 25 μL of Nafion solution (5 wt %) was injected and further sonicated for 30 min. Lastly, 3.0 μL of the prepared ink solution was coated onto the GCE and dried at 50 ℃. For the mass activity of the catalyst, cyclic voltammograms (CVs) were collected by scanning in 1.0 M KOH and 1.0 M ethanol at a scan rate of 50 mV s^{-1} between −0.9 and 0.2 V. The electrochemical active surface areas (ECSAs) were evaluated by scanning in 1.0 M KOH at the same scan rate.

Characterizations. TEM observations were carried on JEOL JEM-2100 with an accelerating voltage of 200 kV. STEM mappings and EDS were performed on FEI Talos F200X apparatuses equipped with STEM and EDS detectors. XRD patterns were carried out on powder samples using a D/max 2500 VL/PC diffractometer (Japan) equipped with graphite-monochromatized Cu Kα radiation. XPS was collected on a scanning X-ray microprobe (Thermo ESCALAB 250Xi) that uses Al Kα radiation, and C 1s peak (284.8 eV) was employed

as a standard to calibrate the binding energies of other elements. ICP-MS was conducted using NexION 350D.

Acknowledgements

D. Xu thanks the financial supports from Natural Science Foundation of Jiangsu Province (BK20191366), National Natural Science Foundation of China (22075147, 21671106), Priority Academic Program Development of Jiangsu Higher Education Institutions, National and Local Joint Engineering Research Center of Biomedical Functional Materials.

Keywords: Porous nanomesh • edge-rich • defects • aqueous synthesis • ethanol electrooxidation

[1] a) X. Ji, K. T. Lee, R. Holden, L. Zhang, J. Zhang, G. A. Botton, M. Couillard, L. F. Nazar, *Nat. Chem.* **2010**, *2*, 286-293; b) M. K. Debe, *Nature* **2012**, *486*, 43-51; c) H. A. Gasteiger, N. M. Marković, *Science* **2009**, *324*, 48-49; d) Y. Zheng, Y. Jiao, A. Vasileff, S. Z. Qiao, *Angew. Chem. Int. Ed.* **2018**, *57*, 7568-7579; e) M. Kamarudin, S. K. Kamarudin, M. Masdar, W. R. W. Daud, *Int. J. Hydrogen Energy* **2013**, *38*, 9438-9453.

[2] a) Z. W. Seh, J. Kibsgaard, C. F. Dickens, I. B. Chorkendorff, J. K. Norskov, T. F. Jaramillo, *Science* **2017**, *355*, eaad4998; b) S. Hu, X. Wang, *Chem. Soc. Rev.* **2013**, *42*, 5577-5594; c) M. Iqbal, Y. V. Kaneti, J. Kim, B. Yuliarto, Y. M. Kang, Y. Bando, Y. Sugahara, Y. Yamauchi, *Small* **2019**, *15*, e1804378; d) C. Zhu, D. Du, A. Eychmuller, Y. Lin, *Chem. Rev.* **2015**, *115*, 8896-8943.

[3] a) Y. Bing, H. Liu, L. Zhang, D. Ghosh, J. Zhang, *Chem. Soc. Rev.* **2010**, *39*, 2184-2202; b) H. Xu, H. Shang, C. Wang, Y. Du, *Adv. Funct. Mater.* **2020**, *30*, 2000793; c) L. Zhang, K. Doyle-Davis, X. Sun, *Energy Environ. Sci.* **2019**, *12*, 492-517; d) P.-F. Yin, M. Zhou, J. Chen, C. Tan, G. Liu, Q. Ma, Q. Yun, X. Zhang, H. Cheng, Q. Lu, B. Chen, Y. Chen, Z. Zhang, J. Huang, D. Hu, J. Wang, Q. Liu, Z. Luo, Z. Liu, Y. Ge, X.-J. Wu, X.-W. Du, H. Zhang, *Adv. Mater.* **2020**, *32*, 2000482.

[4] a) W. Huang, X. Kang, C. Xu, J. Zhou, J. Deng, Y. Li, S. Cheng, *Adv. Mater.* **2018**, *30*, 1706962; b) H. Lv, L. Sun, D. Xu, B. Liu, *Sci. Bull.* **2020**, *65*, 1823-1831; c) S. Ji, Y. Chen, X. Wang, Z. Zhang, D. Wang, Y. Li, *Chem. Rev.* **2020**, *120*, 11900-11955; d) D. Xu, H. Lv, H. Jin, Y. Liu, Y. Ma, M. Han, J. Bao, B. Liu, *J. Phys. Chem. Lett.* **2019**, *10*, 663-671; e) A. Chen, C. Ostrom, *Chem. Rev.* **2015**, *115*, 11999-12044; f) T. J. Wang, F. M. Li, H. Huang, S. W. Yin, P. Chen, P. J. Jin, Y. Chen, *Adv. Funct. Mater.* **2020**, *30*, 2000534; g) M. Luo, Z. Zhao, Y. Zhang, Y. Sun, Y. Xing, F. Lv, Y. Yang, X. Zhang, S. Hwang, Y. Qin, J.-Y. Ma, F. Lin, D. Su, G. Lu, S. Guo, *Nature* **2019**, *574*, 81-85.

[5] a) L. Chen, L. Lu, H. Zhu, Y. Chen, Y. Huang, Y. Li, L. Wang, *Nat. Commun.* **2017**, *8*, 14136; b) C. Li, Q. Yuan, B. Ni, T. He, S. Zhang, Y. Long, L. Gu, X. Wang, *Nat. Commun.* **2018**, *9*, 3702; c) J. Liu, Q. Ma, Z. Huang, G. Liu, H. Zhang, *Adv. Mater.* **2019**, *31*, e1800696.

[6] L. Wang, Z. Zeng, W. Gao, T. Maxson, D. Raciti, M. Giroux, X. Pan, C. Wang, J. Greeley, *Science* **2019**, *363*, 870-874.

[7] a) X. Huang, S. Tang, X. Mu, Y. Dai, G. Chen, Z. Zhou, F. Ruan, Z. Yang, N. Zheng, *Nat. Nanotechnol.* **2011**, *6*, 28-32; b) J. W. Hong, Y. Kim, D. H. Wi, S. Lee, S.-U. Lee, Y. W. Lee, S.-I. Choi, S. W. Han, *Angew. Chem. Int. Ed.* **2016**, *55*, 2753-2758; *Angew. Chem.* **2016**, *128*, 2803-2808; c) Y. Chen, Z. Fan, Z. Zhang, W. Niu, C. Li, N. Yang, B. Chen, H. Zhang, *Chem. Rev.* **2018**, *118*, 6409-6455; d) Y. T. Pan, X. Yin, K. S. Kwok, H. Yang, *Nano Lett.* **2014**, *14*, 5953-5959; e) M. Zareie Yazdan-Abad, M. Noroozifar, A. R. Modaresi Alam, H. Saravani, J. Mater. Chem. A **2017**, *5*, 10244-10249.

[8] a) Y. Yan, X. Li, M. Tang, H. Zhong, J. Huang, T. Bian, Y. Jiang, Y. Han, H. Zhang, D. Yang, *Adv. Sci.* **2018**, *5*, 1800430; b) J. Ge, P. Wei, G. Wu, Y. Liu, T. Yuan, Z. Li, Y. Qu, Y. Wu, H. Li, Z. Zhuang, X. Hong, Y. Li, *Angew. Chem. Int. Ed.* **2018**, *57*, 3435-3438; *Angew. Chem.* **2018**, *130*, 3493-3496; c) H. Yu, T. Zhou, Z. Wang, Y. Xu, X. Li, L. Wang, H. Wang, *Angew. Chem. Int. Ed.* **2021**, *60*, 12027-12031; *Angew. Chem.* **2021**, *133*, 12134-12138; d) Y. Zhao, X. Tan, W. Yang, C. Jia, X. Chen, W. Ren, S. C. Smith, C. Zhao, *Angew. Chem. Int. Ed.* **2020**, *59*, 21493-21498; *Angew. Chem.* **2020**, *132*, 21677-21682; e) W. Zhu, L. Zhang, P. Yang, C. Hu, Z. Luo, X. Chang, Z. J. Zhao, J. Gong, *Angew. Chem. Int. Ed.* **2018**, *57*, 11544-11548; *Angew. Chem.* **2018**, *130*, 11718-11722.

[9] a) X. Qiu, H. Zhang, P. Wu, F. Zhang, S. Wei, D. Sun, L. Xu, Y. Tang, *Adv. Funct. Mater.* **2017**, *27*, 1603852; b) Y. Wang, S.-I. Choi, X. Zhao, S. Xie, H.-C. Peng, M. Chi, C. Z. Huang, Y. Xia, *Adv. Funct. Mater.* **2014**, *24*, 131-139; c) Y. Ma, W. Gao, H. Shan, W. Chen, W. Shang, P. Tao, C. Song, C. Addiego, T. Deng, X. Pan, J. Wu, *Adv. Mater.* **2017**, *29*, 1703460.

[10] a) J. D. Smith, E. Bladt, J. A. C. Burkhart, N. Winckelmans, K. M. Koczkur, H. M. Ashberry, S. Bals, S. E. Skrabalak, *Angew. Chem. Int. Ed.* **2020**, *59*, 943-950; *Angew. Chem.* **2020**, *132*, 953-960; b) H. Lv, Y. Teng, Y. Wang, D. Xu, B. Liu, *Chem. Commun.* **2020**, *56*, 15667-15670; c) X. Yin, X. Liu, Y. T. Pan, K. A. Walsh, H. Yang, *Nano Lett.* **2014**, *14*, 7188-7194.

[11] a) Z. Zhang, G. Ren, Y. Liu, Y. Liang, M. Wang, S. Wu, J. Shen, *Chem. Asian J.* **2019**, *14*, 4217-4222; b) C. Wang, D. P. Chen, X. Sang, R. R. Unocic, S. E. Skrabalak, *ACS Nano* **2016**, *10*, 6345-6353.

[12] a) Z. X. Liang, T. S. Zhao, J. B. Xu, L. D. Zhu, *Electrochim. Acta* **2009**, *54*, 2203-2208; b) Y. Wang, S. Zou, W.-B. Cai, *Catalysts* **2015**, *5*, 1507-1534; c) C. Bianchini, P. K. Shen, *Chem. Rev.* **2009**, *109*, 4183-4206.

[13] a) L. Luo, C. Fu, F. Yang, X. Li, F. Jiang, Y. Guo, F. Zhu, L. Yang, S. Shen, J. Zhang, *ACS Catal.* **2019**, *10*, 1171-1184; b) K.-W. Wang, W.-D. Kang, Y.-C. Wei, C.-W. Liu, P.-C. Su, H.-S. Chen, S.-R. Chung, *ChemCatChem* **2012**, *4*, 1154-1161; c) X. Zhao, L. Dai, Q. Qin, F. Pei, C. Hu, N. Zheng, *Small* **2017**, *13*, 1602970; d) F. Zhao, C. Li, Q. Yuan, F. Yang, B. Luo, Z. Xie, X. Yang, Z. Zhou, X. Wang, *Nanoscale* **2019**, *11*, 19448-19454.

10.1002/chem.202101144

Entry for the Table of Contents

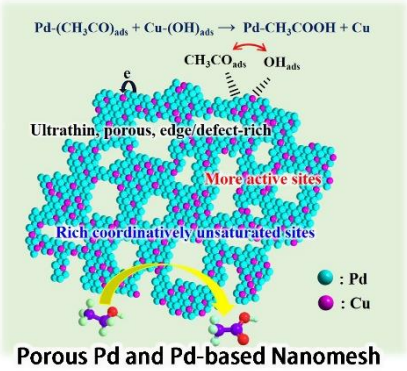

This paper presents a facile and rapid aqueous synthesis for Pd and Pd-alloyed porous nanomesh (PNM) with multiply structural advantages like ultrathin, large-size, porous, edge/defect-rich, ligand-free, resulting in more catalytic active sites and high atomic efficiency. Synergic structural and compositional enhancement effects endowed $Pd_{87}Cu_{13}$ PNM with enhanced mass activity, anti-poisoning ability, and stability/durability in electrocatalytic EOR, compared to PdCu PNM with other elemental ratios, Pd PNM, and Pd NPs.